Experimental study of symmetric and asymmetric shock-shock interactions with variable inflow Mach numbers

Santiago Patterson, Jaime; Laguarda Sanchez, Luis; Schrijer, Ferdinand; van Oudheusden, Bas; Hickel, Stefan

Publication date
2019

Document Version
Accepted author manuscript

Published in
54th 3AF International Conference AERO2019 At: Paris, France

Association Aéronautique et Astronautique de France

54th 3AF International Conference on Applied Aerodynamics
25 — 27 March 2019, Paris – France

FP48-AERO2019-santiago

EXPERIMENTAL STUDY OF SYMMETRIC AND ASYMMETRIC SHOCK-SHOCK INTERACTIONS WITH VARIABLE INFLOW MACH NUMBERS

J. Santiago Patterson, L. Laguarda Sanchez, F.F.J. Schrijer, B.W. van Oudheusden and S. Hickel
Aerospace Engineering Department, Delft University of Technology,
Kluyverweg 1, 2629 HS Delft (The Netherlands), jaimesantiagopatterson@gmail.com

ABSTRACT

An experimental investigation of shock-shock interactions has been conducted with the aim of studying the transition between Regular (RI) and Mach (MI) interactions induced by a variation of the inflow Mach number. The experiments were conducted in the TST-27 wind tunnel at Delft University of Technology. For all cases, the wind tunnel runs were initialized in the RI domain after which the Mach number was slowly decreased to the MI domain, thereby traversing the whole dual solution domain. The process was then inverted to reach again the RI domain in order to investigate a possible transition hysteresis. Both conventional Schlieren and Focusing Schlieren systems were used to visualize the shock wave patterns. The recorded Schlieren images allow accurate transition detection together with quantitative measurements of the Mach Stem Heigth (MSH). The results show no hysteresis effects. All transitions are recorded to occur at the von Neuman line, for both RI to MI and MI to RI cases.

1. INTRODUCTION

When two steady, planar shock waves intersect, a shock-shock interaction is generated. When the shocks are from opposite families, the resulting interaction can be classified as two types: Regular Interaction (RI) or Mach Interaction (MI). Although significant progress has been made in the last half century, the transition process between the two types of interactions remains until today as a research topic of interest in the field of Gas Dynamics. Shock interactions occur on a regular basis in high speed aerodynamic applications such as the propulsion systems of supersonic and hypersonic vehicles or the exhaust nozzles of rocket engines. To be able to progress and improve the design of this type of vehicles, a more complete understanding of the shock interaction phenomenon is crucial. These interactions depend on three main sets of variables: the incidence angle of the shock generators (θ_1 and θ_2), the free stream Mach number (M_0) and the fluid properties. The great majority of existing experimental studies have focused on investigating the effect of changes in θ_1 and θ_2 at a fixed M_0. The main goal of the present study is to investigate the complimentary case, where θ_1 and θ_2 are kept constant and M_0 is varied, a situation that resembles transient flight conditions, such as in the case of an accelerating supersonic vehicle. The analysis of the shock pattern and transition between RI and MI is performed with a robust image processing procedure which shows a great improvement compared to the more subjective methods used in previous studies.

1.1 Theoretical Background

A schematic representation of the two main types of shock-shock interactions, RI and MI, is shown in Figure 1. As can be seen, a RI consists of only oblique shocks with one slipline while a MI contains a quasi-normal shock segment at the reflection point, referred to as the Mach stem, and two sliplines after the normal shock. Initially, these two sliplines form a converging duct that, once they interact with the expansion fans emanating from the trailing edge of the wedges, will curve to form a convergent-divergent duct. This nozzle shaped duct is essential for accelerating the flow back to supersonic velocities.

The existence of an RI or a MI for a given flow configuration is determined by three parameters: θ_1, θ_2 and

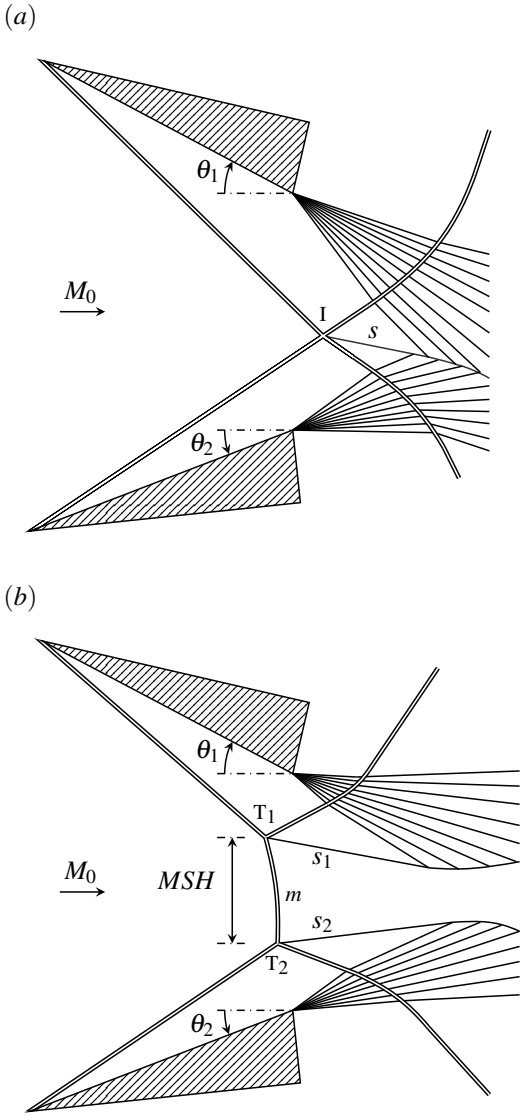

Figure 1: Schematic representation of a Regular Interaction (a) and a Mach Interaction (b).

M_0. At the same time, the Mach Stem Heigth (MSH) also depends on the $2g/w$ length scale, where $2g$ represents the vertical distance between the trailing edges of the wedges and w the hypotenuse length of the wedges. A complete explanation of how these parameters can be used to predict the resulting shock interaction configuration can be found in [13] and [1]. In essence, if θ_1 and θ_2 are fixed, there are two extreme M_0 values, that determine the limits for which only an RI or a MI is possible. Above the von Neuman Mach number (M_{VN}), only RI configurations are possible. On the other hand, below the Detachment Mach number (M_D) only MI systems are physically stable. An additional region exists for M_0 values that satisfy $M_D < M_0 < M_{VN}$ known as the dual solution domain. In this region, both RI and MI configurations are physically possible. A representation of these three domains for a given $M_0 - \theta_1$ can be seen in Figure 3. The study of the physical mechanisms that determine the transition between RI and MI is still an open problem and has been the research topic of many studies.

1.2 State of the art

One of the first studies on the topic of shock-shock interactions and the transition process between RI and MI is [7]. Here, it was hypothesized that the transition in both directions must happen at the von Neuman condition in order to satisfy the mechanical equilibrium condition, and that RI configurations could not exist beyond. It was later shown in [10] and [2] that a hysteresis loop can exist, placing the transition point from RI to MI at the Detachment condition and the MI to RI transition at the von Neuman one. This loop was not experimentally observed until years later through the study in [11]. In this investigation, it was shown that the full hysteresis loop can only be observed under low noise conditions and that perturbations in the flow, which are common in supersonic wind tunnels, play a crucial role in the transition point location.

The disappearance of the hysteresis loop once disturbances reach a certain magnitude is usually attributed to the fact that the MI configuration tends to be more stable than the RI within the dual solution domain. A number of studies have been performed with the goal of further investigating this hypothesis. In [6], shock polar theory is used to derive the higher stability of the MI versus the RI in the dual solution domain. [16] found, through the injection of controlled amounts of water vapor in the test section, that even very small perturbations in the flow can trigger premature transition from RI to MI.

All of the mentioned studies analyzed the transition process by varying θ_1 or θ_2. Up to date, there are only two previous investigations which focused on the complimentary case, where θ_1 and θ_2 are constant and M_0 is variable: [9] and [3]. The former analyzed the problem with a numerical approach. It was found that the transition points for the variable M_0 case follow a similar trend as the variable θ_1, θ_2 case with RI to MI transition happening a the Detachment condition and MI to RI at the von Neuman condition. The main difference in this representation is that these conditions are now expressed in terms of Mach number (M_D and M_{VN}) instead of deflection angle (θ_D and θ_{VN}). Reference [3] performed the only previous experimental investigation on the topic. Here, the effect of changing the inflow Mach number for both symmetric and asymmetric wedge configurations was investigated, with the goal of finding and characterizing the hysteresis loop. No hysteresis loop was found, with most transition points happening halfway through the dual solution domain. The absence of any hysteresis phenomenon is again attributed to the presence of noise and free stream disturbances within the test section.

The previous experimental results for a variable M_0 are still very limited, with only a few number of cases available, and not rigorous enough to fully understand the phenomenon. The current paper aims to expand this line of research by providing more elaborate and complete results on the topic. This will be done by a thorough analysis of the Mach Stem evolution and precise measurements of the transition point for several geometries. In most of the previous studies, the transition point was determined in a subjective way by visual inspection of the resulting images. In this case, it is done through a precise image processing analysis where the Mach Stem Height and the transition points are computed in a more systematic way.

2. METHODOLOGY

2.1 Experimental facilities and setup

The experiments were carried out in the transonic-supersonic TST-27 wind tunnel, located at the High Speed Laboratory of the TU Delft Aerospace Engineering Faculty. This is a blowdown type facility with a test section of 270 x 280 mm and a variable nozzle throat that allows Mach number variations during a run. The facility can generate Mach number ranges of 0.5 to 0.85 and 1.15 to 4.2 in the transonic and supersonic regimes, respectively. The total pressures used during the experiments ranged from 4 bar to 6 bar, depending on the specific start-up requirements for each configuration. The total temperature was kept at ambient temperature at approximately 280 K.

A schematic representation of the test model is shown in Figure 2. It consists of two wedges placed opposite to each other, one facing upwards and the other downwards. This way they act as two shock generators creating shock waves from opposite families that intersect in the center of the test section, generating the desired shock-shock interaction configuration. Both wedges are rigidly connected to the side walls of the test section through two horizontal supports. The top wedge was kept unchanged for all experiments while the bottom one could be interchanged between five different geometries, allowing a constant θ_1 and a θ_2 that could be changed in a discrete way. Both wedges span the complete width of the test section with the aim of minimizing three dimensional effects and any influence of the tips on the interaction region. The parameter that defines the shock-expansion fan pattern geometry is $2g/w$. This ratio was kept constant during all experimental runs at a value of $2g/w = 1.79$ and $w = 42$ mm. These parameters were determined together with the expected M_0 ranges in order to eliminate any interaction between the expansion fans and the interaction point and to avoid the impingement of any reflected shocks on the wedges, which could result in an unstart of the system.

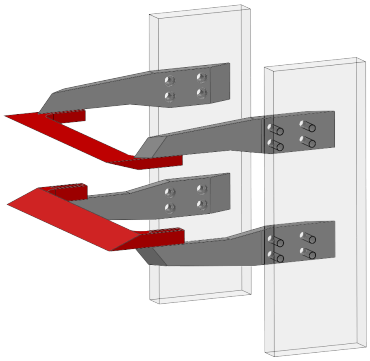

Figure 2: Three dimensional schematic representation of the wind tunnel model used. The setup shown contains the wedges for the $\theta_1 = 17°$, $\theta_2 = 22°$ configuration.

The experimental parameter space is defined through the θ_1, θ_2 angles and the M_0 range used in each run. The selection of θ_1 determines the shape of the von Neuman and Detachment curves on the $M_0 - \theta_2$ plane and the size of the dual solution domain. θ_1 was set at 17° as a compromise value which generated a sufficiently wide dual solution domain within the possible M_0 ranges the tunnel could generate but not high enough for it to become a problem during the startup process. Four of the θ_2 configurations, $\theta_2 = 22°, 21°, 19°$ and 17°, were selected to allow shock systems within the dual solution domain, while the fifth $\theta_2 = 10°$ was chosen in order to provide an experiment without any dual solution domain. The experimental $M_0 - \theta_2$ plane corresponding to the selected θ_1 configuration, together with the M_0 ranges and θ_2 angles used for the experiments are shown in Figure 3. As it will be later explained in section 3.4, a noticeable deviation was found between the design θ_1 and θ_2 values and the actual angles measured during the wind tunnel tests. For the remaining of the paper the nominal angles will be referred to as θ_{1N} and θ_{2N} and the actual angles measured at transition as θ_{1T} and θ_{2T}.

Each experiment was started at the highest M_0 value for that specific run, within the RI domain, to facilitate the start up process of the tunnel. Once the test section reached a steady state, M_0 was then slowly reduced all the way to its lowest value traversing the whole dual solution domain (in the cases where it exists) to reach the MI domain. The process was then reversed until reaching again the initial M_0 condition with the objective of searching for hysteresis effects. Each experiment was repeated five times in order to increase the statistical significance of the results.

2.2 Flow Measurement techniques

The value of M_0 was obtained during the experiments by using two pressure ports located on both sides of the test section and one located in the settling chamber. This way

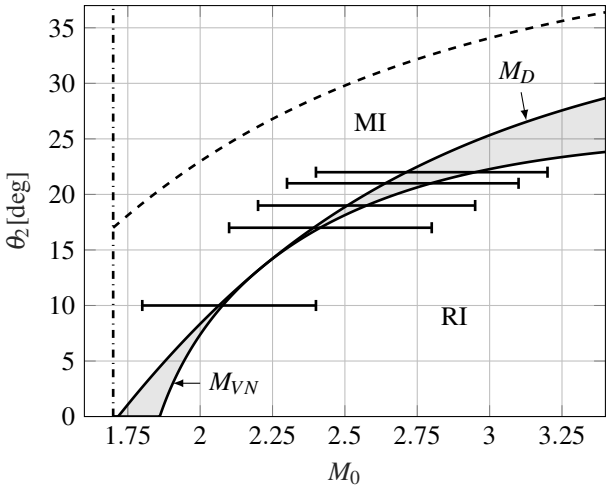

Figure 3: $M_0 - \theta_2$ plane for $\theta_1 = 17^\circ$ showing the dual solution domain in the shaded area. The θ_2 and θ_1 attached shock boundaries are shown through the dashed and dash-dotted lines, respectively. M_{VN} represents the von Neuman curve and M_D the Detachment one. The M_0 ranges used in the experiments are represented through the black horizontal segments.

it was possible to obtain continuous static and total pressure readings at a frequency of 5000 Hz during the whole run, allowing the calculation of instantaneous M_0 values through isentropic flow relations.

The two flow visualization techniques used were conventional Schlieren and Focusing Schlieren. Conventional Schlieren was used as the main tool for the study, as it allowed a precise determination of the shock pattern at every instant of the run. The light source was generated with a continuous white lamp, which was collimated through a mirror that generated a parallel beam that traversed the test section. The final Schlieren image was generated with a vertical knife configuration. In the case of the $\theta_{2N} = 10^\circ, 17^\circ$ and 19° experiments, the images were recorded with a LaVision High Speed 4M camera at a rate of 125 Hz and an exposure time of 100 µs. In the case of the $\theta_{2N} = 21^\circ$ and $\theta_{2N} = 22^\circ$ experiments, the camera used was a LaVision Imager sCMOS at a frame rate of 50 Hz and an exposure time of 100 µs. All images were obtained at a resolution of 2016×2016 pixels.

A main disadvantage of any Schlieren setup is that, due to its infinite depth of focus, the recorded images are a composition of all the density gradients present in the test section integrated over the full span of the test section. This means that any undesired imperfections or flow features, such as three dimensional effects near the edges, will contaminate the final image. A Focusing Schlieren setup can eliminate these unwanted features by reducing the depth of focus to a thin slice around the plane of interest [15]. A Focusing Schlieren setup was built in order to provide a qualitative idea of the influence of these unwanted effects on the images obtained through the traditional Schlieren system, and thus assist in the interpretation of the visualization results of the latter system. The Focusing setup consists of a light source, a pair of source and cutoff grids and a camera lens. All of the images were recorded with a LaVision Imager sCMOS camera at a frame rate of 50 Hz, an exposure time of 30 µs and a resolution of 2016×2016 pixels. The optical characteristics of a Focusing Schlieren system are determined by the grids, the focusing lens and the relative distance between components [17]. The parameters used for the current setup are shown in Table 1. All of the geometries were tested with a fixed focal plane in order to compare the resulting images with those obtained with the regular Schlieren setup. In order to get a better insight of the flow topology of a MI system, an additional run was performed for a single geometry where the focal plane was slowly shifted through the test section in the spanwise direction while keeping a stable MI configuration.

Table 1: Main parameters of the Focusing Schlieren setup used.

A	83 mm	Lens aperture
f	250 mm	Focal length of lens
l	550 mm	Distance from plane of interest to lens
L	1100 mm	Distance from source grid to lens
l'	458 mm	Distance from lens to image plane
L'	323 mm	Distance from lens to cutoff grid
b	1.6 mm	Width of dark strips on the source grid

3. RESULTS AND DISCUSSION

3.1 Focusing Schlieren and three-dimensional effects

A comparison of two images obtained with the Schlieren and Focusing Schlieren systems for the same M_0 and $\theta_1 - \theta_2$ geometry is shown in Figure 4. The plane of focus of the Focusing setup was calibrated to be in the center of the test section, which maximizes the distance from any three dimensional effects generated at the walls. As it can be seen, both techniques clearly capture all of the main flow elements of the MI, namely the incident and reflected shocks, the expansion fans, the Mach stem and the sliplines, although there are some noticeable differences. The most important one is that image (a) shows the shocks in a much thicker way than image (b). The reason for this is that the Focusing system is capable of only showing the flow features present at the plane of focus, while keeping everything else out of focus. On the other hand, the Schlieren system not only captures the shocks present in the plane of interest but also any flow features present anywhere along the span of the test section, in-

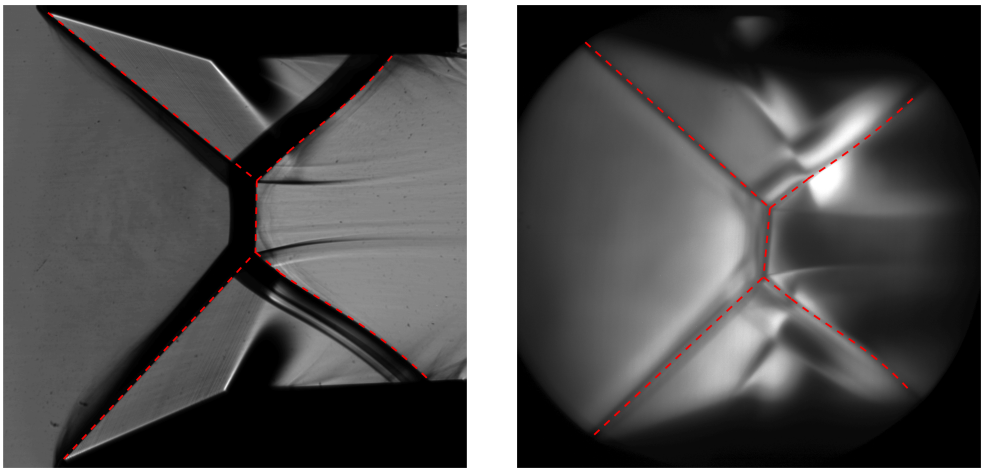

(a) (b)

Figure 4: A comparison of two MI images obtained through the Schlieren (a) and Focusing Schlieren (b) visualization systems. Both images were obtained for the $\theta_{1N} = 17°$, $\theta_{2N} = 22°$ configuration at $M_0 = 2.45$. The shock pattern, including the incident and reflected shocks and the Mach stem, is highlighted through the dashed red lines.

cluding the side walls. By comparing both images, it can be seen how the shocks captured with the Focusing system correspond with the downstream edges of the black lines captured at the shock location in the Schlieren image. It can then be inferred that the rest of these lines must be attributed to flow effects near the walls. During the experiments, it was seen how these additional features had a more unsteady behavior than the actual shocks. This indicates that they are likely to be generated by an unsteady source, such as a turbulent or detached boundary layer. This leads to the conclusion that these additional features are probably generated by a boundary layer detachment at the walls, caused by the negative pressure gradients imposed by the shocks. In previous works, such as [12] and [16], shock patterns, caused by tip effects, containing both MI and RI at different points along the span of the wedges were observed. After shifting the focal plane of the Focusing Schlieren system to regions near the walls, no such patterns were found in the current setup, probably due to the fact that the wedges covered the full span of the test section, minimizing this way the effect of the tips. Therefore, it can be concluded that the only significant three dimensional effects present in the current setup is the boundary layer separation present at the walls. In order to minimize the error introduced by these effects, only the downstream edge of the shocks were considered when processing the Schlieren images.

3.2 Schlieren visualization

Figure 5 shows the shock pattern evolution of a typical experimental run, obtained with the Schlieren visualization system for the $\theta_{1N} = 17°, \theta_{2N} = 22°$ configuration. The run starts at the maximum M_0 value, within the RI domain, where a clear RI shock pattern can be seen in subfigure (a). The incident shocks interact in the center of the image generating the reflected shocks that are later curved due to the effect of the expansion fans. Due to the asymmetry of the wedges, a slipline is generated separating the two distinct regions behind the reflected shocks. As M_0 is reduced, the incident shock angles increase and the transition point is reached, as shown in subfigure (b). At this point, the Mach stem is still too small to be appreciated in the image, but a second slipline can be seen appearing in a darker color than the previous ones. The emergence of this second slipline can be considered a clear sign of the transition from RI to MI. The reason for the change in color of the sliplines is that, due to the creation of the normal shock, the density difference between the flow within the stream tube and the flow outside it is increased. This change in density creates a sharper gradient, detected by the Schlieren system as a darker line. As M_0 is further decreased and the system moves deeper into the MI domain, the size of the Mach stem increases, which can be clearly seen in subfigure (c). At this point, the convergent-divergent duct formed by the sliplines behind the reflected shocks is distinctly shown. The straight lines that emanate from the triple points slowly become curved as they interact with the expansion fans, forming the familiar convergent-divergent nozzle shape. This effect is consistent with the expected theoretical behavior presented in Section 1.1. The Mach stem reaches its maximum size at the minimum M_0, resulting in the shock pattern shown in subfigure (d). As M_0 is increased again, the opposite process is observed, with the size of the Mach stem slowly decreasing to finally disappear and return to the initial state in subfigure (a). It is important to notice how the shock patterns are

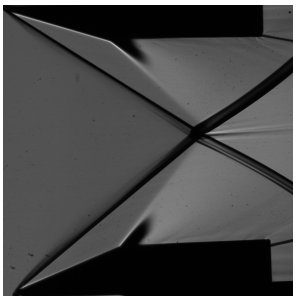

(a) $M_0 = 3.19$.

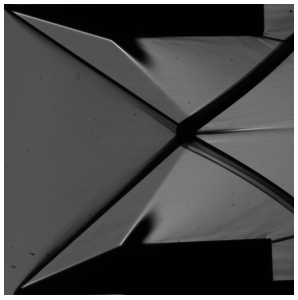

(b) $M_0 = 2.95$, decreasing.

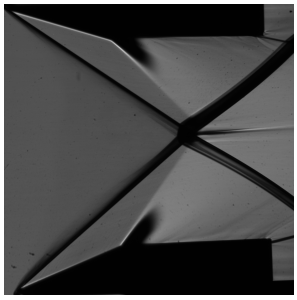

(f) $M_0 = 2.95$, increasing.

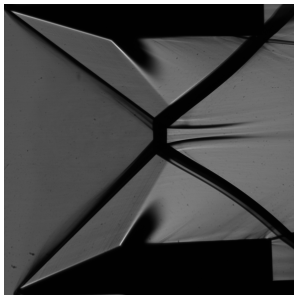

(c) $M_0 = 2.66$, decreasing.

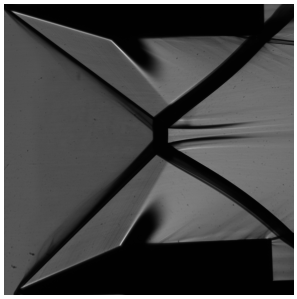

(e) $M_0 = 2.66$, increasing.

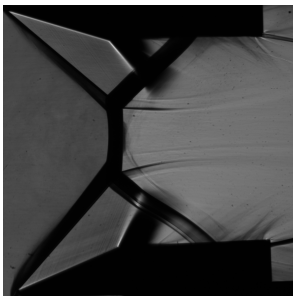

(d) $M_0 = 2.38$

Figure 5: Sequence of Schlieren images showing the shock pattern evolution for the $\theta_{1N} = 17^\circ$, $\theta_{2N} = 22^\circ$ geometry. The left column shows the image for the decreasing M_0 leg of the run and the right column the increasing M_0 one.

identical at every instant and the transition point is detected at the same M_0 value. This can be considered as a first indication of the non-existence of the hysteresis loop within the current experimental setup.

3.3 Mach Stem Height evolution

The recorded evolution of the MSH, normalized with the wedge hypotenuse (w), is shown in Figure 6. The MSH evolution was computed for all runs within each geometry and it was found that the variation of this curve between runs was minimal. For this reason and for the sake of clarity, only one run per geometry is shown in Figure 6. The MSH was computed for every image within each run by processing the Schlieren images. This was done by capturing the incident shocks and analyzing the shock pattern near the intersection point. The resulting MSH was then combined with the wind tunnel pressure measurements to link every MSH value to its corresponding M_0. The resulting error for MSH/w is estimated to be in the order of 10^{-2}.

An important feature to notice in Figure 6 is how there is an almost perfect overlap of the MSH/w curves for increasing and decreasing M_0. The ratio of dM_0/dt to the characteristic time scale scale of the problem, computed as $\frac{dM_0/dt}{u_\infty/w}$ is in the order of 10^{-5}. This indicates that the rate of change of M_0 was negligible compared to the time scales of the flow. Under these conditions, the experiments performed can be analyzed under the assumption of quasi-steady flow. This way, although M_0 is varying in time, each snapshot of the flow can be assumed to be representing a steady state. Under these steady state conditions, the size of the MSH at a given M_0 is determined by θ_1, θ_2 and $2g/w$ [14]. θ_1, θ_2 and $2g/w$ were kept constant within each run, so the only possible range in which the MSH could take different values depending on if M_0 is increasing or decreasing is the dual solution domain. If a hysteresis loop exists, a different MSH curve would be observed for increasing and decreasing M_0 in the dual solution domain region. Because all of the the MSH curves show a clear overlap in all geometries, it can be concluded that a hysteresis loop was not detected in the present study.

Two different types of MSH evolution curves can be seen near the transition points. In the case of the $\theta_{2N} = 17^\circ, 19^\circ, 21^\circ$ and 22° geometries, it is clear that once the M_0 reaches the transition point, the MSH rapidly changes from zero to a finite value and then follows a smooth trend all the way to the maximum MSH value and back. In the case of the $\theta_{2N} = 10^\circ$ the transition happens in a smooth way, with the MSH evolving without any sharp jumps near the transition point.

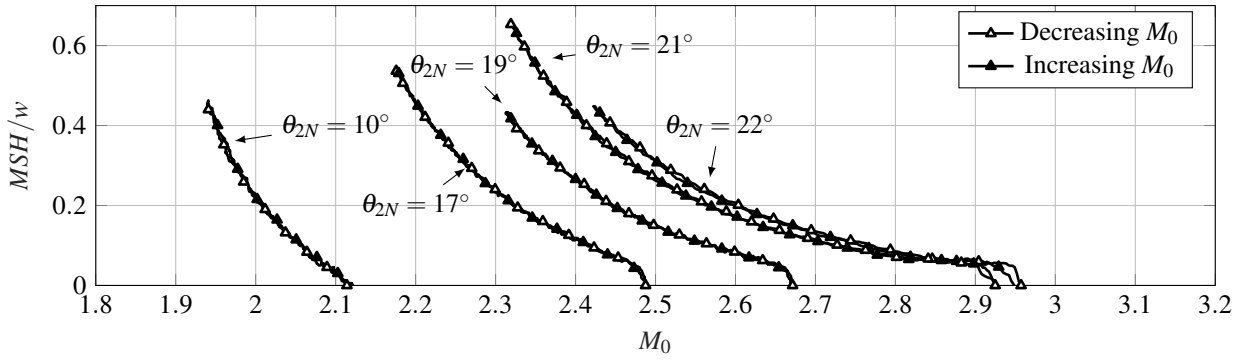

Figure 6: Evolution of the normalized MSH with M_0 for all geometries.

Table 2: Transition values obtained for all geometries. Each θ_{1T}, θ_{2T} and M_{0T} value is computed as the average of the five runs completed for each geometry.

		RI to MI			**MI to RI**		
θ_{1N} [deg]	θ_{2N} [deg]	θ_{1T} [deg]	θ_{2T} [deg]	M_{0T}	θ_{1T} [deg]	θ_{2T} [deg]	M_{0T}
17.0	22.0	16.0	22.9	2.95	15.9	22.8	2.95
17.0	21.0	16.0	22.5	2.92	15.9	22.4	2.92
17.0	19.0	16.4	20.4	2.67	16.3	20.4	2.67
17.0	17.0	16.5	18.3	2.49	16.4	18.2	2.48
17.0	10.0	16.9	11.4	2.11	16.9	11.3	2.11

3.4 Transition and hysteresis

The transition point for each run was determined through the MSH evolution measurements. A shock interaction was assumed to have transitioned from RI to MI when the MSH length exceeded a minimum threshold. A transition from MI to RI was assumed to happen in the opposite scenario when the MSH reached a value below the previously established threshold. This threshold value was established at $MSH/w = 0.01$ which, as explained before, it is the estimated uncertainty of the MSH/w computation. Applying this criterion, the transition Schlieren image for each run was obtained. The M_0 value at transition (M_{0T}) could then be determined by linking these Schlieren transition images to their corresponding M_0 at that given instant. The remaining parameters needed to completely characterize the transition points are θ_1 and θ_2 at transition (θ_{1T} and θ_{2T}). As mentioned in Section 2.1, during the experiments and the processing of the results it was found that there was a non-negligible deviation of the actual deflection angles from the nominal ones for which the experiments were designed. This deviation is attributed to wedge deformations caused by the large loads applied on the model and boundary layer development over the surface of the wedges. To account for this, θ_{1T} and θ_{2T} were determined in an indirect way. For this, the shock angles at transition (ϕ_{1T} and ϕ_{2T}) were computed by capturing the shocks in the corresponding images. ϕ_{1T} and ϕ_{2T}, combined with M_{0T} allowed to obtain the corresponding θ_{1T} and θ_{2T} angles through the Rankine Hugoniot relations. It is estimated that the error of the θ_{1T} and θ_{2T} angles obtained through this method is in the order of $0.6°$. This procedure was applied to all the runs performed during the experimental campaign, the results obtained are visually presented in Figure 7. In this plot, the von Neuman and Detachment lines were computed by using the average θ_{1T} value recorded for all runs and geometries. The individual results for each geometry are shown in Table 2.

The first thing that can be noticed in Figure 7 is that there is an excellent repeatability of the results, which can be seen through the almost perfect overlap of the transition points detected at different runs within each geometry. At the same time, it can be noticed how the RI to MI and MI to RI points also match almost exactly within every run. This is another clear indication that no hysteresis effects were present in the current experiments, which is consistent with the MSH evolution results previously discussed in Section 3.3. It can also be seen very clearly how all of the transition points lie almost exactly on the von Neuman line. In the $\theta_{2N} = 10°$ case, the von Neuman point transition is expected. As it has already been mentioned, the current experiment can be considered as a quasi-steady system. Under these circumstances, and given the absence of any dual solution domain for $\theta_{2N} = 10°$, there is only one possible transition point, which is the von Neuman point. The excellent agreement with this theoretical prediction and the mea-

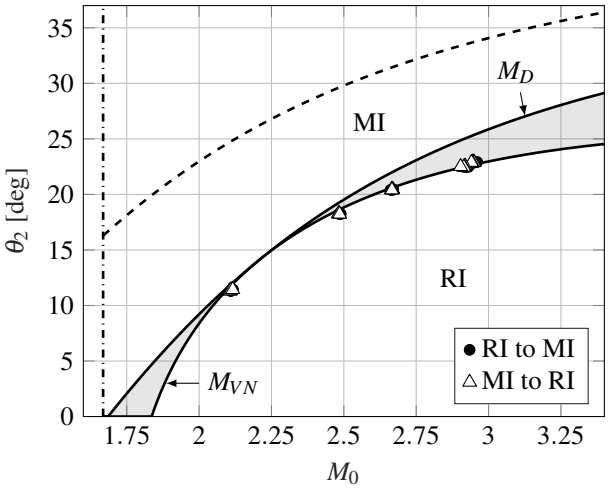

Figure 7: $M_0 - \theta_2$ plane for $\theta_1 = 16.3^\circ$ together with the detected transition points of all runs. The dual solution domain is shown through the shaded area and the θ_2 and θ_1 attached shock boundaries through the dashed and dash-dotted lines, respectively.

sured result is a convincing validation of the transition detection method used to obtain the present results.

For the rest of the geometries ($\theta_{2N} = 17^\circ, 19^\circ, 21^\circ$ and 22°), if a perfect uniform flow is assumed, a transition at the Detachment line for the RI to MI cases and at the von Neuman line for the MI to RI, as reported in [11], would be expected. As it can be clearly seen in Figure 7, this is not the case, with all the transition points lying on the von Neuman line and no hysteresis loop detected. The reason for this is suspected to be the non-uniformities and noise present in the flow. The wind tunnel used, unlike the one in [11], cannot be considered a low-noise facility [4]. There are previous studies, such as [5] or [8], where transition was also always detected at the von Neuman point. Other studies, such as [16] indicate that small free stream perturbations can play a crucial role on the premature transition from RI to MI. In light of the present results, it is likely that the perturbations and noise generated by the TST-27 wind tunnel are high enough to trigger a premature transition from RI to MI resulting in a transition on the von Neuman line in both directions.

4. CONCLUSIONS

Experiments on shock-shock interactions have been performed with the aim of analyzing the effect of a variable inflow Mach number on the evolution of the Mach stem and the transition between Regular and Mach interactions. Two flow visualization techniques were used: conventional Schlieren and Focusing Schlieren. The Focusing Schlieren system was capable of removing most three dimensional effects from the resulting images. At the same time, it revealed that the main three dimensional effect present in the setup is likely a boundary layer detachment at the walls and that any tip effects were negligible. The Schlieren images allowed an accurate determination of the Mach Stem Height evolution for five different deflection angle combinations. These results showed an absence of any hysteresis effects with an identical evolution of the MSH for both increasing and decreasing Mach numbers in all geometries. A sharp jump in the size of the Mach stem was detected at transition for geometries that traversed the dual solution domain. These MSH evolutions were used to determine the transition points between RI and MI of all geometries. The results showed a very good experimental repeatability with all transition points lying on the von Neuman line and no hysteresis loop even in the presence of a wide dual solution domain. These results are attributed to the presence of significant flow perturbations generated by the wind tunnel.

REFERENCES

[1] G. Ben-Dor. *Shock Wave Reflection Phenomena*, chapter 1, General introduction. Springer-Verlag, 1992.

[2] A. Chpoun, D. Passerel, H. Li, and G. Ben-Dor. Reconsideration of oblique shock wave reflections in steady flows. Part 1. Experimental investigation. *Journal of Fluid Mechanics*, 301:19–35, 1995.

[3] A. Durand, B. Chanetz, R. Benay, and A. Chpoun. Investigation of shock waves interference and associated hysteresis effect at variable-mach-number upstream flow. *Shock Waves*, 12:469–477, 2003.

[4] R.H.M. Giepman, F.F.J. Schrijer, and B.W. van Oudheusden. High-resolution PIV measurements of a transitional shock wave-boundary layer interaction. *Experiments in Fluids*, 56(113), 2015.

[5] L.F. Henderson and A. Lozzi. Experiments on transition of Mach reflexion. *Journal of Fluid Mechanics*, 68(1):139–155, 1975.

[6] H.G. Hornung. On the stability of steady–flow regular and Mach reflection. *Shock Waves*, 7:123–125, 1996.

[7] H.G. Hornung, H. Oertel, and R.J. Sandeman. Transition to Mach reflexion of shock waves in steady and pseudosteady flow with and without relaxation. *Journal of Fluid Mechanics*, 90:541–560, 1979.

[8] H.G. Hornung and M.L. Robinson. Transition from regular to Mach reflection of shock waves. Part 2. The steady-flow criterion. *Journal of Fluid Machanics*, 123:155–164, 1982.

[9] M.S. Ivanov, G. Ben-Dor, T. Elperin, A.N. Kudryavstev, and D.V. Khotyanovsky. Flow Mach number variation induced hysteresis in steady shock wave reflections. *AIAA Journal, Technical Notes*, 39(5), 2000.

[10] M.S. Ivanov, S.F. Gimelshein, and A.E. Beylich. Hysteresis effect in stationary reflection of shock waves. *Physics of Fluids*, 7(4):685–687, 1995.

[11] M.S. Ivanov, A.N. Kudryavtsev, S.B. Nikiforov, D.V. Khotyanovsky, and A.A. Pavlov. Experiments on shock wave reflection transition and hysteresis in low-noise wind tunnel. *Physics of Fluids*, 15(6):1807–1810, 2003.

[12] M.S. Ivanov, D. Vandromme, V.M. Fomin, A.N. Kudryavstev, A. Hadjadj, and D.V. Khotyanovsky. Transition between regular and Mach reflection of shock waves: new numerical and experimental results. *Shock Waves*, 11:199–207, 2001.

[13] H. Li, A. Chpoun, and G. Ben-Dor. Analytical and experimental investigations of the reflection of asymmetric shock waves in steady flow. *Journal of Fluid Mechanics*, 390:25–43, 1999.

[14] C.A. Mouton and H.G. Hornung. Mach stem height and growth rate predictions. *AIAA Journal*, 45(8):1977–1987, 2007.

[15] G.S. Settles. *Schlieren and Shadowgraph Techniques: Visualizing Phenomena in Transparent Media*. Springer-Verlag Berlin Heidelberg, 2001.

[16] N. Sudani, M. Sato, T. Karasawa, J. Noda, A. Tate, and M. Watanabe. Irregular effects on the transition from regular to Mach reflection of shock waves in wind tunnel flow. *Journal of Fluid Mechanics*, 459:167–185, 2002.

[17] L.M. Weinstein. Review and update of lens and grid schlieren and motion camera schlieren. *The European Physical Journal Special Topics*, 182:69–95, 2010.